ARTICLE   OPEN

An energetics tale of the 2022 mega-heatwave over central-eastern China

Tuantuan Zhang[1,2], Yi Deng[3], Junwen Chen [4 ✉], Song Yang [1,2] and Yongjiu Dai[1,2]

It remains a major challenge to attribute heatwave's lifecycle characteristics quantitatively to interwoven atmospheric and surface actions. By constructing a process-resolving, energetics-based attribution framework, here we quantitatively delineate the lifecycle of the record-breaking 2022 mega-heatwave over central-eastern China from a local energetics perspective. It is found that the cloudlessness induced radiative heating and atmospheric dynamics dominate the total energy buildup during the developing stage, while the land-atmosphere coupling and atmospheric horizontal advection act most effectively to sustain and terminate the heatwave, respectively. A reduction in anthropogenic aerosols provides a persistent positive contribution during the event, suggesting that pollution mitigation measures may actually increase the amplitudes of future heatwaves. With this framework, initial efforts are made to unravel culprits in a model's sub-seasonal prediction of this mega-heatwave, demonstrating the framework's potential for efficiently detecting the origins of climate extremes and quantitatively assessing the impacts of mitigation policies for sustainable development.

INTRODUCTION

Heatwaves pose widespread yet disproportionate threats to the ecosystems and human well-being across the globe, and these associated adverse effects are further exacerbated by mega-heatwaves with long durations and large amplitude[1–5]. Central-eastern China, with accelerating climate change and population aging, is particularly vulnerable to increasing and intensifying heatwaves[6–8]. In the mid-to-late summer of 2022, a record-breaking mega-heatwave roasted broad swathes of China, among which the central-eastern region is considered the hardest-hit (Fig. 1). This "heatwave from the hell" with scorching temperature exceeding 40 °C at some stations, superimposed by droughts and wildfires, is among the most severe recorded in global history[9,10]. Close to one billion people were affected by the scorching hot, as well as the heatwave-caused energy crisis, i.e., water and electricity shortages[10]. Given that more deadly heatwaves are projected in the future, quantifying the casual factors of mega-heatwave and further disentangling the origin of the uncertainties of heatwave prediction can provide impact-based decision-making support for disaster mitigation and prevention[11–14]. While several studies attributed the extremely hot summer in 2022 to extra-tropical atmospheric circulation, tropical sea surface temperature, and local soil moisture–temperature feedback, the latter being a comprehensive quantitative attribution of the multiple dynamical and radiative drivers on the occurrence of this mega-heatwave is absent[15–20]. In fact, this attribution gap exists in almost the entire research community for climate and weather extremes.

Typically, the development, maintenance, and attenuation of heatwaves involve both dynamical and radiative processes[21–27]. During the development and maintenance of a certain heatwave, a high-pressure system that produces clear skies allows more solar radiation to reach the ground, inducing an anomalous surface warming[21,25]. Upward surface heat fluxes are thus generated,

along with adiabatic subsidence, leading to an increase in air temperature, maintaining the local high-pressure system and hence the heatwave[21,25]. Collapses of the high-pressure system and local land-atmosphere feedback contribute to the termination of heatwave[21,25]. In addition to these typical processes, the evolution of heatwave may also be modulated by the radiative processes associated with the changes in aerosols and water vapor, among others[28,29]. For example, an increased amount of aerosols can reduce the surface temperature and hence the probability of heatwave occurrence through absorption or scattering of shortwave radiation, and vice versa[24]. Given the well-recognized processes associated with the lifecycle of heatwaves mentioned above, a fundamental question remains: What are the relative roles of those dynamical and radiative processes in the different phases of heatwaves?

According to the total energy balance equation, the temperature change-induced longwave cooling is balanced by multiple physical processes in an equilibrium state. In light of such a premise, several climate attribution methods including but not limited to the partial radiative perturbation method[30] (PRP) and the coupled atmosphere–surface climate feedback–response analysis method[31,32] (CFRAM), have been developed to quantify the contributions from individual processes to radiative forcings at the top of the atmosphere/surface and to air/surface temperatures changes from seasonal to decadal time scales[33–37]. However, these methods are not applicable in a non-equilibrium state, where weather and climate extreme events lie in. On the other hand, the moist static energy (MSE) budget[38] with energy unbalanced, which is an indicative of total energy budget, has been intensively adopted to quantify the contributions from physical processes in the lifecycle of intra-seasonal oscillation (e.g., Madden–Julian Oscillation and boreal summer intra-seasonal oscillation)[39–41]. Furthermore, the shortwave and longwave radiative forcings could be decomposed into partial perturbations associated with

[1]School of Atmospheric Sciences, Sun Yat-sen University; Southern Marine Science and Engineering Guangdong Laboratory (Zhuhai), 519082 Zhuhai, China. [2]Guangdong Province Key Laboratory for Climate Change and Natural Disaster Studies, Sun Yat-sen University, Zhuhai 519082 Guangdong, China. [3]School of Earth and Atmospheric Sciences, Georgia Institute of Technology, Atlanta, GA 30319, USA. [4]Shenzhen Wiselec Technology Co., Ltd., Shenzhen 518048 Guangdong, China. ✉email: junwen.chen@wiselec.cn
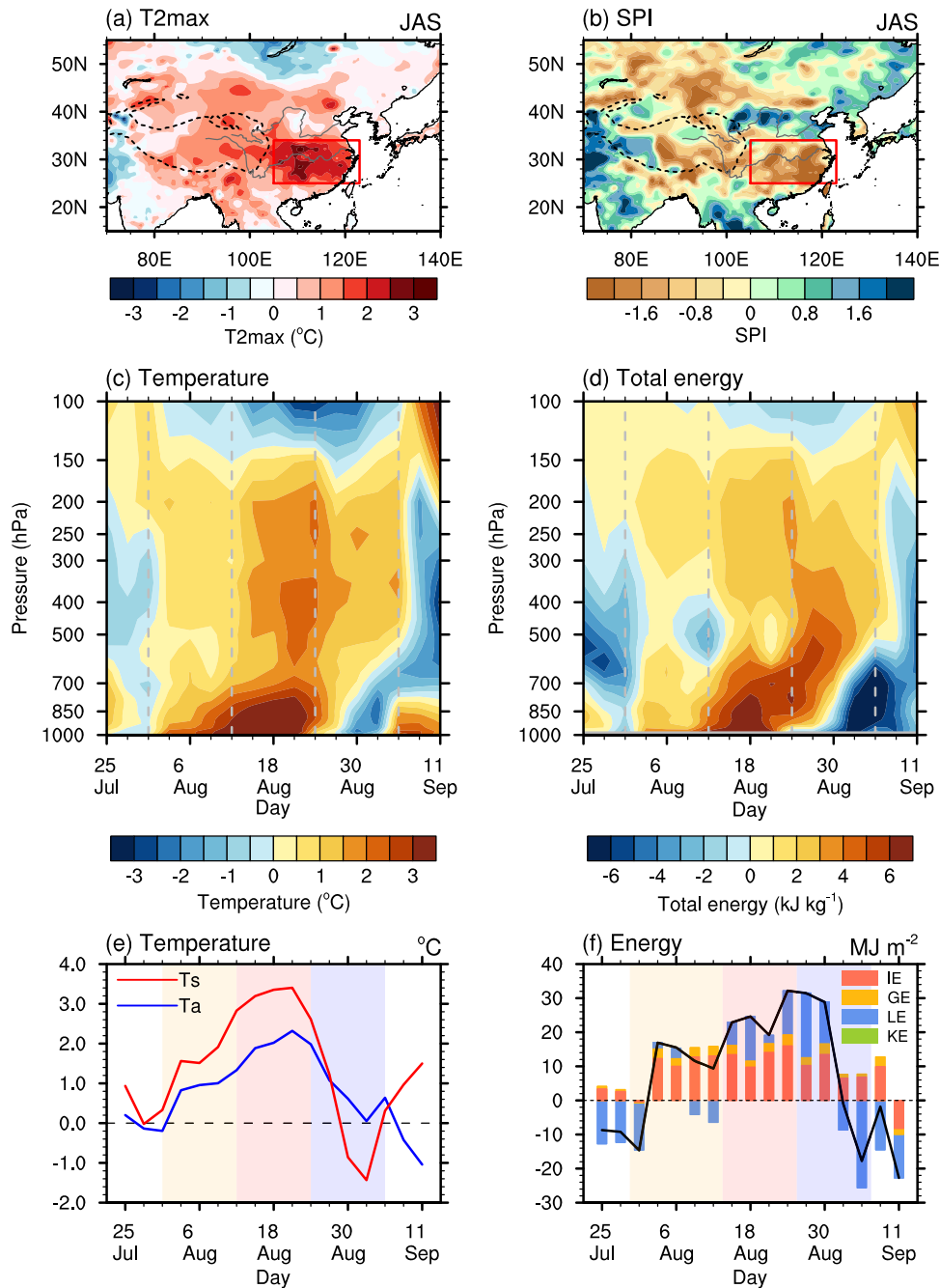
Fig. 1 Evolutions of temperature and energy associated with the 2022 mega-heatwave over central-eastern China. Spatial patterns of (**a**) maximum 2-m air temperature anomalies (°C) and (**b**) 3-month Standardized Precipitation Index in the 2022 mid-late summer (July–September), and time-pressure cross sections of (**c**) air temperature (°C) and (**d**) total energy (kJ kg^{-1}) anomalies averaged over central-eastern China (105°–123°E, 25°–34°N). Shown also are the time series of area-averaged central-eastern China (**e**) land surface temperature (°C; red line) and column-mean (from surface to 150 hPa) air temperature (°C; blue line), plus (**f**) column integrated (from surface to 150 hPa) total energy (MJ m^{-2}; black line) and its components of internal energy (coral), geopotential energy (orange), latent energy (blue), and kinetic energy (green). The domain of central-eastern China is outlined by the red box in (**a**, **b**). The developing, mature, and decaying phases of the heatwave are marked by vertical dashed lines in (**c**, **d**), and by pale yellow, light pink, and light blue shadings in (**e**, **f**).

different physical processes through linearization as proposed by the PRP and the CFRAM, which has been adopted to study regional or global weather and climate events[42–49]. The changes in temperature during different phases of heatwaves are directly linked to the recharge-discharge of internal energy, which is the dominant part of the total energy in the atmosphere. This provides an insight to dissect the heatwaves from the energetics perspective, which can attribute total energy (i.e., MSE plus kinetic

energy) change into multiple dynamical and radiative processes according to the total energy budget equation together with the linearization concept in deriving individual radiative perturbations from the PRP and the CFRAM.

In this study, a comprehensive process-resolving, energetics-based attribution framework (PREAF) is developed to quantify the contributions from multiple physical processes associated with atmospheric dynamics (i.e., horizontal advection and vertical

advection), surface latent and sensible heat fluxes, and radiative drivers (i.e., solar insolation, ozone, surface albedo, temperature, water vapor, cloud, and aerosols) to the lifecycle of the 2022 mega-heatwave over central-eastern China. An initial effort is also made to unravel the culprits of the heatwave sub-seasonal prediction biases by evaluating model performance for these quantified contributions. This framework is able to fulfill the attribution and predictability analysis of any specific heatwave, which is expected to substantially facilitate the operational prediction of heatwaves and thereby provide benefits for heatwave prevention and mitigation.

RESULTS

Detecting the 2022 mega-heatwave over central-eastern China from an energetics perspective

In the mid-to-late summer (July–September) of 2022, the daily maximum 2 m air temperature was 2 °C above normal and the 3-month Standardized Precipitation Index (SPI) was lower than −1.6 over most of central-eastern China (105°–123°E, 25°–34°N), indicating extremely hot and drought conditions (Fig. 1a, b). Climatologically, central-eastern China was a hotspot of heatwave occurrence, and the number of heatwave days (>40 days) reached the peak in the summer of 2022 since 1980 (Supplementary Fig. 1). As such, the 2022 heatwave here has come into focus.

Several heatwaves in central-eastern China in 2022 have been identified (in early July, late July–late August, and early September), and we focus mainly on the one from late July to late August, which was the most intense and prolonged event (Supplementary Fig. 2). Proceeded by a moderate and short-lived cooling, warm anomalies dominated almost the entire troposphere from 31 July to 27 August, with an intense warming transported upward from the planetary boundary layer to the tropopause (Fig. 1c and e). The warm anomalies were terminated by an intense cooling originated from the low-level troposphere afterwards (Fig. 1c and e). Apparently, the warming during this heatwave was not limited to the near surface, and we thus investigate the processes associated with the changes in both the land surface temperature and the atmospheric air temperature from a land-atmosphere coupling perspective.

The evolution of total energy anomalies bears a large resemblance to that of temperature (Fig. 1c–f), since the dominant part of total energy, i.e., the internal energy, is directly calculated using temperature (Fig. 1f), and the contribution of latent energy associated with water vapor is gradually increasing which plays a secondary role in total energy variations (Fig. 1f). Given that heatwaves amplified by humid conditions (namely moist heatwave) may exert exacerbated effects than dry heatwaves, it is acceptable to consider both the internal and latent energy for the evolution of heatwaves. The upward transportation of positive anomalies during the heatwave period, and the transition from positive to negative anomalies around 27 August are also observed for total energy (Fig. 1d and f). Therefore, the 2022 mega-heatwave over central-eastern China can also be detected from an energetics perspective. According to the evolution of area-averaged land surface temperature anomalies, atmospheric air temperature anomalies (averaged from surface to 150 hPa), and the total energy anomalies (integrated from surface to 150 hPa), the lifecycle of this mega-heatwave is classified into three stages: the developing phase characterized by a rapid increase in temperature and total energy from 30 July to 13 August, the mature phase depicted by a peak and a maintenance of temperature and total energy from 14 August to 25 August, and the decaying phase with a rapid drop in temperature and total energy from 26 August to 6 September (Fig. 1e, f). Since then, the evolution of the heatwave can be interpreted as the recharge-discharge of total energy, and an energy-level quantitative

attribution of the heatwave to multiple dynamical and radiative processes can be conducted.

Process-resolving, energetics-based quantitative attribution

The recharge-discharge process of total energy is determined by the changes in energy tendency. That is, positive total energy tendency signifies an increase in total energy and vice versa. Utilizing the PREAF constructed in this study (see Methods), the total energy tendency attributed to individual dynamical and radiative processes is derived and used to quantify the relative contribution of each process in the lifecycle of the 2022 mega-heatwave (Figs. 2–3). An energetics tale of this mega-heatwave is elaborated as follows.

During the developing phase of this mega-heatwave, the positive total energy tendency of land surface is dominated by radiative processes (Fig. 2a), which are associated with a nearly equivalent barotropic anticyclone occupying central-eastern China (Supplementary Fig. 3a, d, and g). The developing and strengthening of the anticyclone are linked to the eastward eddy shedding from the Asian monsoon anticyclone (AMA) in the upper troposphere (Supplementary Fig. 4), which leads to intensified negative vorticity advection downstream at the upper troposphere that drives initial sinking motion and the formation of low-level anticyclone, resulting in westward extension of the western North Pacific subtropical high[50–52] (Supplementary Fig. 3d). This anticyclonic eddy shedding event seems to be an atmospheric dynamical trigger of the mega-heatwave, which dominates the rapid buildup of total energy at the beginning of developing phase through strong positive vertical advection (i.e., adiabatic heating due to descent motions) and horizontal advection (Fig. 2c). The induced anomalous anticyclonic circulation leads to a decrease in low-level clouds with less cloud water (Supplementary Fig. 5a, b) and allowing more solar radiation (shortwave) to reach the land surface (Supplementary Fig. 6a). As shown in Fig. 2b, which further presents the total energy tendency attributed to individual radiative processes, the changes in cloud provide a dominant positive contribution, while the processes associated with aerosols play a secondary positive role. The reduced aerosols (indicated by negative anomalies of aerosol optical depth shown in Supplementary Fig. 5i) contribute to an increase in surface incoming radiation during the entire lifecycle of the mega-heatwave, and the shortwave effects of black carbon and sulfate are the main contributors (Supplementary Fig. 7a, c, and e). The shortwave heating to the land surface is partially compensated by the longwave cooling through emitting more longwave radiation from the warming surface associated with temperature feedback (Fig. 2b and Supplementary Fig. 6b). As the surface warming enhanced, accompanied by continuously reduced soil moisture and precipitation (Supplementary Fig. 5c, d), surface latent and sensible heat fluxes tend to transport more energy from the land surface to the atmosphere, providing negative contributions for the total energy tendency of land surface (Fig. 2a, Supplementary Fig. 5e, f).

The increase in total energy of the atmosphere during the developing phase is mainly induced by the positive horizontal advection associated with the anomalous anticyclonic circulation and the positive forcings from surface latent and sensible heat fluxes (Fig. 2c). On the other hand, the radiative processes provide an overall negative contribution (Fig. 2c), among which the longwave effect linked to the decrease in cloud water and precipitable water plays a dominant role (Fig. 2d, and Supplementary Figs. 5–6). The changes in aerosols also provide a considerable negative contribution (Fig. 2d), driven primarily by the shortwave effect of reduced black carbon through absorbing less solar radiation (Supplementary Figs. 6–7).

During the mature phase, the radiative processes associated with clouds and aerosols persistently contribute most to the positive total energy tendency of the land surface (Fig. 2a). As precipitable water increases (Supplementary Fig. 5g), the
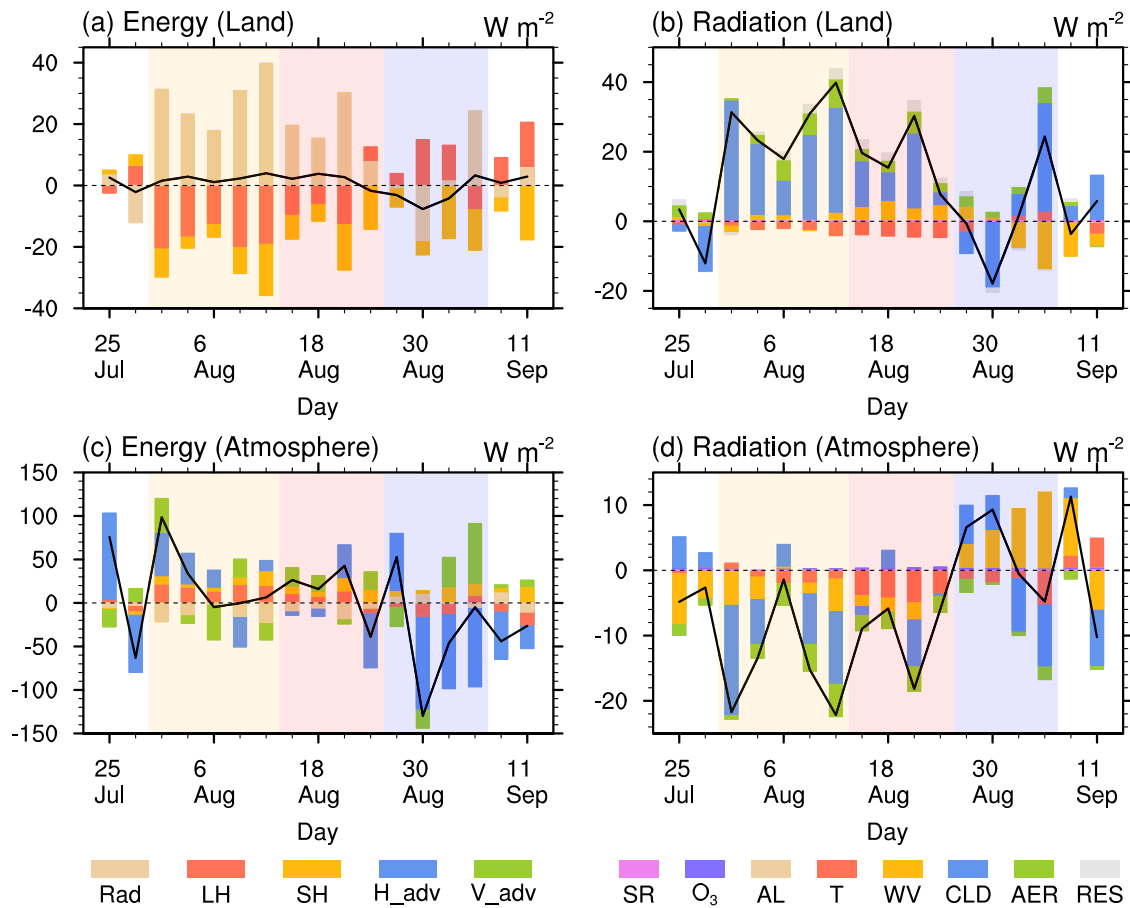
Fig. 2 Quantitative attribution of the 2022 central-eastern China mega-heatwave to multiple dynamical and radiative processes. The energy perturbations (W m^{-2}) of (**a**) land surface and (**c**) atmosphere attributed to the dynamical and radiative processes during the life cycle of the heatwave, and the radiative energy perturbations of (**b**) land surface and (**d**) atmosphere associated with different radiative processes. The abbreviations "RAD", "LH", "SH", "H_adv", and "V_adv" in (**a**) and (**c**) stand for the processes of radiation, surface latent heat flux, surface sensible heat flux, horizontal advection, and vertical advection, respectively. The abbreviations "SR", "O$_3$", "AL", "T", "WV", "CLD", "AER", and "RES" in (**b**) and (**d**) stand for the processes of the changes in solar insolation, ozone, surface albedo, temperature, water vapor, cloud, aerosols, and residual, respectively. The black line in (**a**) and (**c**) denotes the total energy tendency (W m^{-2}) of land surface and atmosphere, respectively. The black line in (**b**) and (**d**) represents the total energy tendency (W m^{-2}) of land surface and atmosphere contributed by the radiative processes. The developing, mature, and decaying phases of the heatwave are marked by pale yellow, light pink, and light blue shadings. **c** and **d** Are the results of column integration from surface to 150 hPa.

longwave effect (i.e., "greenhouse effect") of water vapor becomes more important during the mature phase and provides a considerable positive effect (Fig. 2b and Supplementary Fig. 6b). The increase in water vapor is possibly associated with the precipitation deficit (leaving more water vapor in the atmosphere) and the positive transportation by the southerly anomalies (Supplementary Figs. 3b, 5c, 5g, and 5h). The negative contribution from surface latent and sensible heat fluxes taken energy from the land surface to the atmosphere is similar with that in the developing phase (Fig. 2a, Supplementary Fig. 5e,f). There is a weakening effect of surface latent heat flux due to the continuously drying of soil in the mature phase, and an intensifying effect of surface sensible heat flux due to the continuously rising of surface temperature (Fig. 2a and Supplementary Fig. 5d–f). On the contrary, surface latent and sensible heat fluxes provide considerable positive contributions to the total energy of the atmosphere (Fig. 2c). The positive vertical advection also plays an important role in the maintenance of total energy (Fig. 2c), which is likely related to the intensified anticyclone that provides adiabatic heating due to the descent motions in the mature phase (Supplementary Fig. 3b, e, and h). The positive total energy tendency of the atmosphere is partially compensated by the negative effects of the radiative processes associated with the

longwave cooling of the changes in cloud, water vapor, and temperature and the shortwave cooling of the changes in aerosols (Fig. 2c, d and Supplementary Fig. 6c, d).

The decaying phase of the mega-heatwave is characterized by a rapid decrease in total energy associated with the negative tendency (Figs. 1f, 2a, and 2c). In this stage, the low-level anomalous anticyclonic circulation is replaced by an anomalous cyclonic circulation, and northerly anomalies dominate over central-eastern China (Supplementary Fig. 3c). As a result, the radiative heating of the land surface is terminated primarily by the increased low-level clouds with more cloud water (Fig. 2a, b and Supplementary Fig. 5a, b). The upward anomalous surface sensible heat flux generated by persistently warm surface contributes considerably to the negative total energy tendency of the land surface, whereas the downward anomalous surface latent heat flux associated with a relief of precipitation deficit and dry soil provides a positive tendency (Fig. 2a and Supplementary Fig. 5c–f). Opposite effects of sensible and latent heat fluxes are observed in the atmosphere (Fig. 2c). The horizontal advection (cold advection) associated with northerly anomalies plays a dominant role in the negative total energy tendency of the atmosphere, partially compensated by the positive vertical advection associated with the anticyclone in the mid-upper
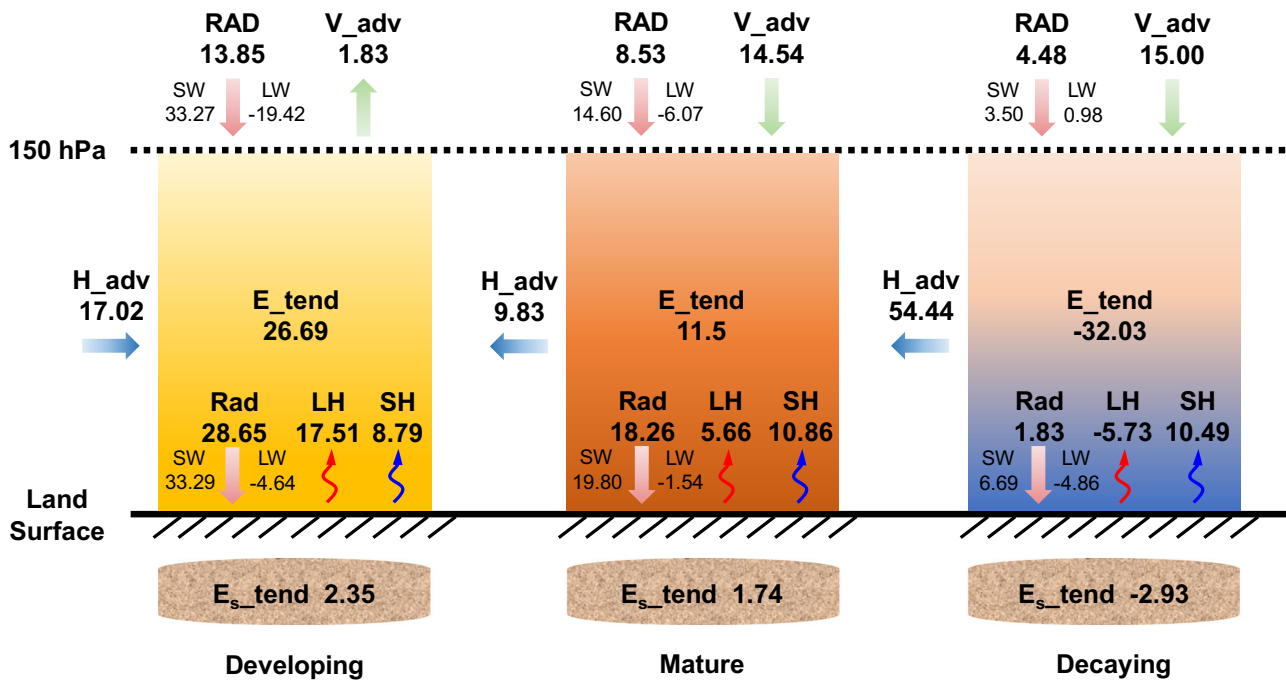
Fig. 3   A schematic diagram with the specific quantitative energy transport anomalies in the land-atmosphere column during the life cycle of the mega-heatwave over central-eastern China. The abbreviations "RAD", "SW", "LW", "LH", "SH", "H_adv", "V_adv", and "E$_s$_tend", "E_tend" stand for processes of radiation, shortwave radiation, longwave radiation, surface latent heat flux, surface sensible heat flux, horizontal advection, vertical advection, and the total energy tendency of land surface and atmosphere, respectively. The specific quantitative energy transport associated with the individual dynamical and radiative processes is displayed by the directed numbers. The direction of the arrows represents positive energy transport.

troposphere (Fig. 2c and Supplementary Fig. 3c, f, and i). The effects of the radiative processes associated with the changes in cloud, water vapor, temperature, and aerosols tend to compensate each other, providing an overall weak effect (Fig. 2c, d).

A schematic diagram with the specific quantitative energy transport anomalies is displayed in Fig. 3. During the developing phase, the land surface receives a net shortwave radiative heating of 33.29 W m^{-2} and a net longwave radiative cooling of 4.64 W m^{-2}. The radiative processes thus provide an overall 28.65 W m^{-2} heating to the land surface, which is compensated by the negative contributions of upward surface latent (17.51 W m^{-2}) and sensible heat fluxes (8.79 W m^{-2}), leaving a total of 2.35 W m^{-2} energy tendencies in the land surface. Although there is a net incoming radiative heating of 13.85 W m^{-2} at the tropopause (150 hPa), more radiative heating (28.65 W m^{-2}) is transported from the atmosphere to the land surface, leading to an energy loss of 14.85 W m^{-2} in the atmosphere by the radiative processes. The horizonal advection imports 17.02 W m^{-2} total energy perturbations to the atmo-sphere, while the vertical advection exports 1.83 W m^{-2}. As a result, a total of 26.69 W m^{-2} energy tendencies for the atmo-sphere is observed. During the mature phase, the 1.74 W m^{-2} total energy tendencies in the land surface is a result of the net radiative heating (18.26 W m^{-2}) and the export of surface latent (5.66 W m^{-2}) and sensible (10.86 W m^{-2}) heat fluxes. For the atmosphere, the total energy perturbations provided by vertical advection (14.54 W m^{-2}) and latent (5.66 W m^{-2}) and sensible (10.86 W m^{-2}) heat fluxes are partially compensated by the export of energy associated with radiative processes (net radiative heating of 8.53 W m^{-2} at the tropopause while net radiative cooling of 18.26 W m^{-2} at the land surface) and horizontal advection (9.83 W m^{-2}), resulting in 11.5 W m^{-2} total energy tendencies. During the decaying phase, sensible heat flux imports 10.49 W m^{-2} energy perturbations from the land surface to the

atmosphere, and radiative processes (1.83 W m^{-2}) and downward surface latent heat flux (5.73 W m^{-2}) provide energy perturbations of 7.56 W m^{-2} to the land surface, inducing a negative total energy tendency of −2.93 W m^{-2} for the land surface. On the other hand, the negative total energy tendency of −32.03 W m^{-2} in the atmosphere can be primarily attributed to horizontal advection (−54.44 W m^{-2}), which is compensated partially by the import of total energy associated with radiative processes (4.48 W m^{-2}–1.83 W m^{-2} = 2.65 W m^{-2}), surface heat fluxes (10.49 W m^{-2}–5.73 W m^{-2} = 4.76 W m^{-2}), and vertical advection (15 W m^{-2}).

An initial effort disentangling the sources of uncertainties of sub-seasonal heatwave prediction

Sub-seasonal prediction of heatwaves is a huge challenge even for state-of-the-art climate models[53–55], and the main culprits at the process-level remain undiscovered. Even if perfect prediction results are obtained, it is still unknown whether the high skill stems from the accurate representations of various physical processes, or actually a result from the error cancellation among misrepresented processes. Utilizing the PREAF, we take an initial effort to unravel the agreement or discrepancy of the total energy tendency attributed to these processes between observation and model prediction, which can serve as a direct measure of the models' performance in predicting the heatwave.

The forecast of the National Centers for Environmental Prediction (NCEP) Climate Forecast System version 2 (CFSv2) initialized at 0600 UTC 26 July 2022 is evaluated. The developing phase of the mega-heatwave characterized by upward transporta-tions of warm anomalies and positive total energy anomalies is well reproduced by the CFSv2 (Fig. 4 vs Fig. 1). However, the heatwave decays earlier, around 15–25 August, in the model, accompanied by a counterfactual cooling transported downward from the upper-level atmosphere (Fig. 4a). Therefore, the lifecycle
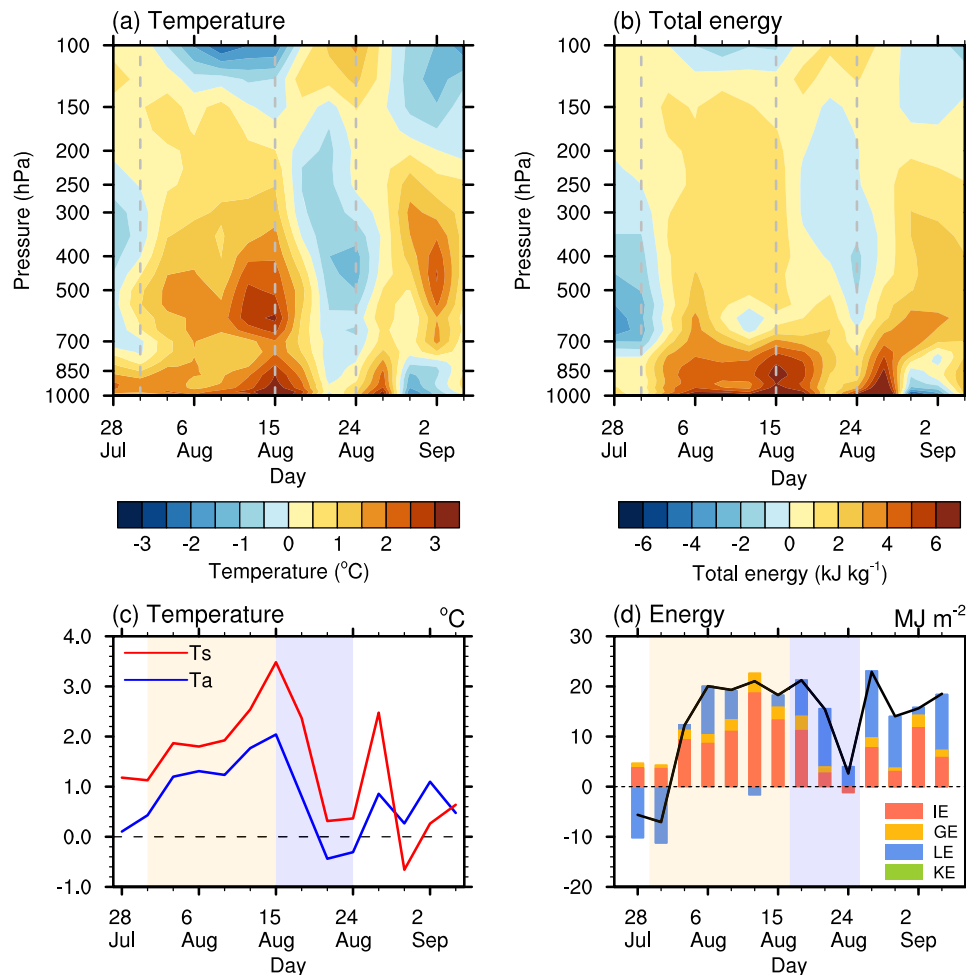
Fig. 4 Sub-seasonal prediction of the mega-heatwave in the NCEP Climate Forecast System version 2 (CFSv2). Time-pressure cross section of (**a**) air temperature (°C) and (**b**) total energy (kJ kg^{-1}) anomalies averaged over central-eastern China in the NCEP CFSv2. Time series of area-averaged central-eastern China (**c**) land surface temperature (°C; red line), column-mean (from surface to 150 hPa) air temperature (°C; blue line), and (**d**) column integrated (from surface to 150 hPa) total energy (MJ m^{-2}; black line) and its components of internal energy (coral), geopotential energy (orange), latent energy (blue), and kinetic energy (green) in the CFSv2. The developing and decaying phases of the heatwave are marked by vertical dashed lines in (**a**, **b**), and by pale yellow and light blue shadings in (**c**, **d**).

of the predicted mega-heatwave is classified into two stages in the model: the developing phase from 30 July to 16 August, and the decaying phase from 17 August to 25 August (Fig. 4c, d).

Figure 5 shows the total energy tendency attributed to multiple radiative and dynamical processes during the developing and decaying phases in both the CFSv2 and observation. It demonstrates that the high prediction skill for the mega-heatwave developing phase originates from the model's fidelity in representing the various physical processes (Fig. 5). The associated anticyclonic circulation and the changes in land surface and atmospheric variables are also well captured during the developing phase (Supplementary Figs. 8–9). On the other hand, the model predicts an opposite effect of surface latent heat flux and opposite transportation of vertical advection compared to observation during the decaying phase (Fig. 5a and c). While the horizontal advection associated with the low-level northerlies dominates the heatwave termination in observation, the vertical advection (i.e., adiabatic cooling) associated with an upper-level anomalous cyclonic circulation contributes largely to the counterfactual cooling over central-eastern China in the CFSv2 (Fig. 5c, and Supplementary Fig. 8b, d, and f). Contrary to the persistently dry soil in observation, the predicted soil moisture increases immediately as a response to the increasing precipitation during

the decaying phase, leading to an opposite sign of surface latent heat flux and a decrease in surface sensible heat flux (Fig. 5a, c and Supplementary Fig. 9c–f). This feature suggests that the land-atmosphere coupling is misrepresented in the CFSv2. Although the positive total energy tendency attributed to radiative processes during the decaying phase is generally captured, the water vapor effect associated with excessive precipitable water is misrepresented in the model (Fig. 5a, b and Supplementary Fig. 9g). The counterfactual cooling induces an opposite radiative effect associated with the temperature changes in the CFSv2 compared with that in observations (Fig. 5d). Overall, the model's infidelity in representing the dynamical and hydrological processes is responsible for the poor performance during the decaying phase. Note that an assessment of the model's performance for the radiative effect of aerosols is not included here due to the lack of aerosol module in the CFSv2.

DISCUSSION
The attribution of regional extreme heat events has attracted a substantial interest under the context of global warming. In this study, we provide compelling evidence to emphasize the necessity of defining heatwaves not only in terms of the near-
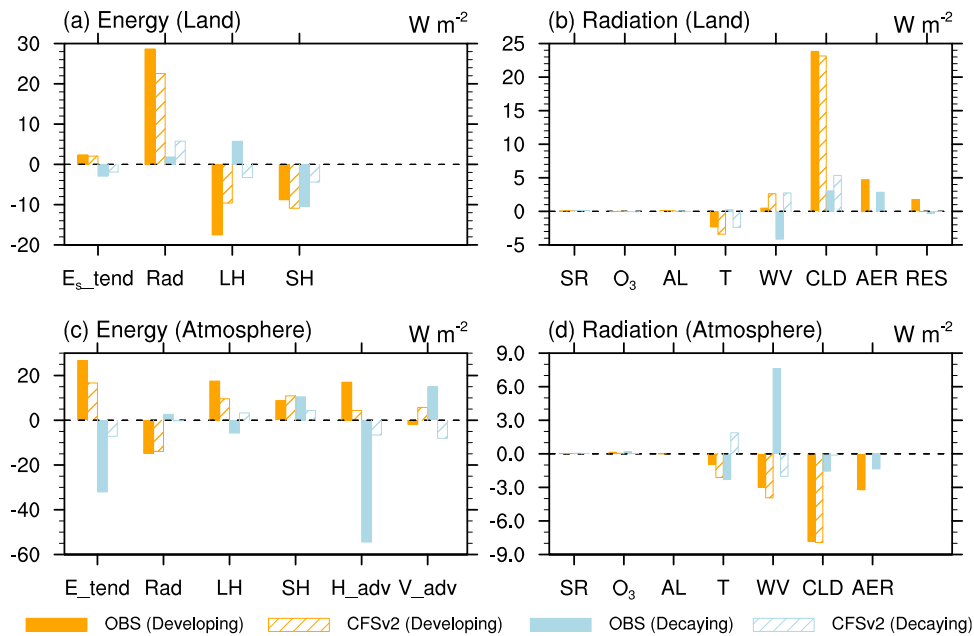
Fig. 5 Quantitatively detecting the origins of the mega-heatwave prediction biases in the NCEP Climate Forecast System version 2 (CFSv2). The energy perturbations (W m^{-2}) of (**a**) land surface and (**c**) atmosphere attributed to the dynamical and radiative processes during the developing (orange) and decaying (light blue) phases of the mega-heatwave in observation (solid) and the CFSv2 (hollow with slashes). The radiative energy perturbations (W m^{-2}) of (**b**) land surface and (**d**) atmosphere decomposed into individual radiative processes. The abbreviations "E_tend", "E$_s$_tend", "RAD", "LH", "SH", "H_adv", "V_adv", "SR", "O$_3$", "AL", "T", "WV", "CLD", "AER", and "RES" in the abscissa stand for the total energy tendency of land surface and atmosphere, processes of the changes in radiation, surface latent heat flux, surface sensible heat flux, horizontal advection, vertical advection, solar insolation, ozone, surface albedo, temperature, water vapor, cloud, aerosols, and residual, respectively.

surface temperature, but also from the energetics and land-atmosphere coupling perspective. This provides a solid basis for further quantitively attributing the 2022 mega-heatwave over central-eastern China to multiple dynamical and radiative processes on the energy level, utilizing an energetics attribution method (namely the PREAF) developed in our study.

The development and termination of this mega-heatwave seem to be mainly driven by atmospheric dynamics originated from the upper and lower troposphere (i.e., eastward shedding eddy and cold air outbreak), while land-atmosphere interaction plays an important role in maintaining the long-lasting heatwave. Accompanied by an equivalent barotropic anticyclonic circulation occupying central-eastern China, the net radiative heating dominated by the short-wave effect of cloud plays a major role in the accumulation of land surface total energy during the developing and mature phases. The shortwave effect associated with reduced aerosols and the long-wave effect associated with enhanced water vapor transport also provide considerable positive contributions. Considering the dominance of the anthropogenic aerosols (i.e., black carbon and sulfate) in the total effects of aerosols, a lower level of aerosol concentration during the 2022 summer is possibly linked to the highly effective policies of emission reduction implemented since 2013 in China. A recent study also reported a positive contribution of reduction in anthropogenic aerosols to the 2016/17 record-breaking warm winter in China[37]. It highlights an important implication that the reduction in anthropogenic aerosols associated with the effective pollution mitigation measures (if taken) could actually facilitate the occurrence of regional heatwaves. As a response to the warm and dry land surface, the enhanced surface heat fluxes bring energy from the land surface to the atmosphere, along with the effects of horizontal advection and vertical advection, contributing to the increase in total energy of the atmosphere. The import of total energy associated with surface latent heat flux to the atmosphere becomes weaker with the dryer soil and changes the sign during the decaying phase, while the persistent positive contribution from the surface

sensible heat flux is observed during the entire lifecycle of the heatwave. The compound hot and drought conditions over central-eastern China in the summer of 2022 provide an ideal background for such a land-atmosphere coupling, and hence favoring the occurrence of long-lasting mega-heatwave. During the decaying phase, the radiative heating of land surface is terminated by a low-level cyclonic circulation, and the negative horizontal energy advection associated with northerlies contributes to the decrease in total energy of the atmosphere.

By comparing the energy perturbations due to the changes in these processes between observations and numerical models, the PREAF can help us objectively detect the origins of the uncertainty of weather and climate predictions. A demo of such a utility of the PREAF is provided based on the forecasts of the CFSv2 initialized at 0600 UTC 26 July 2022, which reproduces the heatwave development well but predicts an earlier-than-observed decay. The excellent performance of the model during the developing phase stems from the accurate representations of the various associated physical processes. On the other hand, the earlier decay of the heatwave in the CFSv2 is owing to the model's infidelity in representing the atmospheric dynamics and hydrological processes. That is, the vertical advection (i.e., adiabatic cooling) associated with an upper-level anomalous cyclonic circulation that does not emerge from observation and an overestimated response of soil moisture to the excessive precipitation contribute largely to the termination of the modeled heatwave. The effects of surface heat fluxes in response to the changes in soil moisture are then also misrepresented. A better performance for key land-atmosphere interactive processes may contribute to advance heatwave prediction. The effect of water vapor, which is opposite in the CFSv2 during the decaying phase compared to the observed, is a source of the prediction bias in other climate models as reported by previous studies[35,56]. The cloud effect seems to be reproduced fairly well by the CFSv2, possibly due to the clear sky during the lifecycle of the 2022

mega-heatwave, which may be a source of prediction uncertainties for other weather and climate events involving cloudy weather or heavy precipitation.

Given its advantage, we recommend applications of the PREAF concept (see Method) to quantitative attributions of multi-scale weather and climate events, including the variations of extreme heat and cold events, intra-seasonal oscillation systems (e.g., MJO), monsoons, El Niño-Southern Oscillation, and so on. Taking into account of the effects of solar irradiance and trace gases such as ozone, CO_2, and CH_4, we can also quantify the contributors to climate change (e.g., global warming) using this efficient, offline, and model-free approach. Addable contributions from the anthropogenic forcing by different species (e.g., ozone, CO_2, and aerosols) and other physical processes will be disclosed. The PREAF thus provides an objective and efficient tool for understanding, predicting, and even projecting extreme weather and climate events, and for assessing the impacts of mitigation policies for sustainable development.

Nevertheless, limitations also exist in this analysis. Firstly, the accuracy of quantitative attribution is limited by the imperfection and deficiency of observational datasets (e.g., reanalysis), in spite of a remarkable improvement of the quality since the satellite era. In particular, it remains an exceptional challenge to obtain datasets of clouds and aerosols with low uncertainty. Secondly, the aerosol module is absent in the CFSv2 (actually in most of the operational sub-seasonal to seasonal models), which limits our understanding of the source of heatwave prediction bias associated with aerosols. Thirdly, this study only provides a preliminary case study of quantifying the causal factors for mega-heatwaves, and the performance of merely one member of the CFSv2 is evaluated. We expect that some certain results will still hold, such as the critical role of land-atmosphere interaction in sustaining mega-heatwaves. Further analysis is needed to examine whether the result is applicable to other mega-heatwaves and numerical models.

METHODS

Observational datasets
The daily maximum 2 m air temperature and precipitation with a resolution of $0.5° \times 0.5°$ are from the in situ observation-based Climate Prediction Center (CPC) global unified temperature and precipitation[57]. The 3-month Standardized Precipitation Index (SPI) is calculated through fitting to a gamma distribution using the CPC precipitation from 2003 to 2022[58,59]. The daily surface actual evaporation and soil moisture (0–10 cm) with a resolution of $0.25° \times 0.25°$ are from the Global Land Evaporation Amsterdam Model (GLEAM) v3.7b[60,61]. The daily cloud fraction from cloud mask, precipitable water (infrared retrieval), cloud liquid water path, and cloud ice water path, combined Dark Target and Deep Blue aerosol optical depth at 550 nm with a resolution of $1° \times 1°$ are from the Level 3 products of MODIS Collection 6.1 (MYD08 from Aqua and MOD08 from Terra)[62]. Note that the mean fields of observations from MODIS/Aqua and MODIS/Terra is used. All the datasets cover the study period of 2003–2022.

Reanalysis datasets
The Modern-Era Retrospective Analysis for Research and Application, version 2 (MERRA-2) is a long-term global atmospheric reanalysis to that assimilates both meteorological and aerosol observations from the U.S. National Aeronautics and Space Administration (NASA)[63], which is considered a proxy for observations. The MERRA-2 has a horizontal resolution of $0.5° \times 0.625°$ and 42 pressure levels in the vertical ranging from 1000 hPa to 0.1 hPa. The daily maximum 2 m air temperature, daily mean surface/air temperatures, specific humidity, geopotential height, zonal and meridional winds, potential vorticity, surface latent and sensible heat fluxes, cloud fractions, cloud liquid/ice water path, precipitation, surface soil moisture (0–5 cm), precipitable water, and aerosol optical depth are adopted

to investigate the physical processes associated with the lifecycle of the 2022 mega-heatwave over central-eastern China. Montgomery streamfunction is defined as $\mathbf{M} = c_p \mathbf{T} + g\mathbf{z}$, where $\mathbf{T}$ is air temperature, $\mathbf{z}$ is geopotential height, c_p is the specific heat of dry air at constant pressure, and g is the gravitational constant. The MERRA-2 has been extensively evaluated with independent observations for both meteorological fields and aerosols around the world[64–66]. The evolution of the associated variables in the MERRA-2 during the lifecycle of the mega-heatwave is consistent with that in observations (Supplementary Fig. 5). Note that the CPC global unified daily precipitation data is used to correct the precipitation in the low and middle latitudes ($|\text{lat}| < 42.5°$, except Africa)[67], resulting in consistent variations of precipitation and surface soil moisture with observations over central-eastern China (Supplementary Fig. 5c,d), although the total cloud fraction increased (primarily the high clouds) during the developing and mature phases in the MERRA-2, which is inconsistent with that in the MODIS observations (Supplementary Fig. 5a). The dominated factors in the calculation of cloud optical properties in the radiative transfer model are the cloud liquid and ice water path, which are consistent with those in the MODIS observations (Supplementary Fig. 5b). Thus, the radiative effects of clouds derived from the MERRA-2 are reliable.

Sub-seasonal prediction of the mega-heatwave
The NCEP CFSv2 is a fully coupled atmosphere–ocean–land model for sub-seasonal to seasonal predictions[68]. The CFSv2 consists of the Global Forecast System atmospheric model with a T126 horizontal resolution (nearly a 100 km grid resolution) and 64 sigma-pressure vertical hybrid levels, the Geophysical Fluid Dynamics Laboratory Modular Ocean Model versions 4 with a nominal 0.5° horizontal resolution and 40 vertical levels, the 4-level Noah land surface model, and an interactive 3-level sea ice model[68]. The 45-day hindcast runs are initialized from every cycle (0000, 0600, 1200, and 1800 UTC) of each day from 1999 to 2010[68]. The 45-day operational runs from 2011 onwards are the same as the hindcast runs, except 4 members are generated for each run[68]. The first member of 45-day forecast initialized at 0600 UTC 26 July 2022 is able to predict a resemble mega-heatwave over central-eastern China. Therefore, this single member forecast is selected as a demo for quantitively assessing the sub-seasonal prediction skill at a process level of this mega-heatwave by utilizing the PREAF. The daily maximum 2 m air temperature, daily mean surface/air temperatures, specific humidity, geopotential height, zonal and meridional winds, surface latent and sensible heat fluxes, cloud fractions, cloud liquid/ice water path, precipitation, surface soil moisture (0–10 cm), and precipitable water are adopted to assess the prediction skill of the mega-heatwave.

Definition of heatwaves
A heatwave is identified when daily maximum 2 m air temperature exceeds the 90th percentile of the daily values in the climatological period of 2003–2022 for at least 3 consecutive days. The number of heatwave days over central-eastern China shown in Supplementary Figs. 1–2 is the area-averaged results during the mid-to-late summer (July–September).

Definition of climatology
The number of assimilated observations has been doubled to about 2-million per 6 h cycle after 2002 in the MERRA-2, benefited from the A-train satellites[63]. The reanalysis quality is substantially improved through assimilating sufficient observations and the uncertainties of model dependent fields (e.g., clouds and aerosols) are further reduced, which are crucial and sensitive in attribution analysis. Furthermore, the interannual variability of heatwave events over central-eastern China is better captured after 2000 (Supplementary Fig. 1c). Therefore, the most recent 20 years

(2003–2022) with more accurate datasets are chosen as the climatology. The anomalies of all variables adopted in this study are calculated by subtracting the daily climatological mean of 2003–2022. The daily climatological mean in the CFSv2 is defined as the average of most recent 20 years in the predictions, i.e., average of the first member of 45-day predictions initialized at 0600 UTC 26 July in each year from 2003 to 2022. The 3-day mean of variables is analyzed to remove the high frequency variability. The 3-day mean from 24 July to 26 July is denoted as day "25 July", and subsequent segments (with 3-day increment each time) of 3-day mean start from 27 July to 29 July (denoted as day "28 July"), 30 July to 1 August ("31 July") … until 10 September to 12 September ("11 September"). All temporal results shown in this study are the mean of 3-day segment, except for Supplementary Fig. 2, where daily values are shown.

The PREAF

The process-resolving, energetics-based attribution framework (PREAF) developed in this study is based on the total energy (i.e., moist static energy plus kinetic energy) budget equation in an atmosphere-land column consisting multiple atmospheric layers and one land surface layer. The total energy of the atmosphere in each layer is defined as:

$$E = c_p T + gz + L_v q + \frac{1}{2}(u^2 + v^2 + w^2) \tag{1}$$

where c_p is the specific heat of dry air at constant pressure, T is air temperature, g is the gravitational constant, z is geopotential height, L_v is the latent heat of vaporization, q is specific humidity, and u, v, and w are zonal, meridional, and vertical velocities, respectively. The four terms on the right-hand side of Eq. (1) represent internal energy, geopotential energy, latent energy, and kinetic energy, respectively. Following the idea of the moist static energy (MSE) budget analysis[39], by taking the difference (Δ) of the vertically-integrated total energy budget equation of the atmosphere between two states ("B" minus "A"), we may express the changes in total energy tendency $\Delta \frac{\partial \langle E \rangle}{\partial t}$ as the sum of energy perturbations due to individual dynamical and radiative processes:

$$\Delta \frac{\partial \langle E \rangle}{\partial t} = -\Delta \left\langle \vec{\mathbf{V_h}} \cdot \nabla \mathbf{E} \right\rangle - \Delta \left\langle \boldsymbol{\omega} \frac{\partial \mathbf{E}}{\partial p} \right\rangle + \Delta \left(SW|_{ptop} - SW|_{surface} \right)$$
$$+ \Delta \left(LW|_{ptop} - LW|_{surface} \right) + \Delta LH + \Delta SH - \Delta Fric \tag{2}$$

where $\vec{\mathbf{V_h}}$ is the horizontal wind, $\boldsymbol{\omega}$ is the vertical velocity in pressure coordinates, SW is the net downward shortwave radiative flux, LW is the net downward longwave radiative flux, LH is the upward surface latent heat flux, SH is the upward surface sensible heat flux, and Fric is the surface friction. Angle brackets indicate the mass-weighted vertical integral in the atmosphere from the surface to ptop. In this study, ptop is set to 150 hPa, which is the top of significant warmings in the atmosphere (Fig. 1 c,d). The difference in total energy tendency between two states can be decomposed into the differences in partial energy perturbations due to (from left to right in the Eq. (2)) horizontal advection, vertical advection, shortwave radiative heating, longwave radiative heating, surface latent heat flux, surface sensible heat flux, and surface friction. For the land surface, we may express the change in total energy tendency $\Delta \frac{\partial E_s}{\partial t}$ (i.e., heat storage of surface layer) as the sum of energy perturbations due to individual dynamical and radiative processes that are coupled with the atmosphere:

$$\Delta \frac{\partial E_s}{\partial t} = \Delta SW|_{surface} + \Delta LW|_{surface} - \Delta LH - \Delta SH \tag{3}$$

Furthermore, the interactions among different radiative-active species are relatively small as proposed by the partial radiative

perturbation method[30] (PRP) and the coupled atmosphere–surface climate feedback–response analysis method (CFRAM)[31,32]. Through linearizing the radiative energy perturbations, we may express the changes in net shortwave and longwave radiative fluxes in each layer as the sum of the changes in partial net radiative energy fluxes due to individual radiative processes (details referred to Zhang et al. [37]):

$$\Delta SW = \Delta SW^{(SR)} + \Delta SW^{(O_3)} + \Delta SW^{(AL)}$$
$$+ \Delta SW^{(WV)} + \Delta SW^{(CLD)} + \Delta SW^{(BC)} + \Delta SW^{(OC)} \tag{4}$$
$$+ \Delta SW^{(SULF)} + \Delta SW^{(SS)} + \Delta SW^{(DUST)} + \Delta res_{SW}$$

$$\Delta LW = \Delta LW^{(O_3)} + \Delta LW^{(Temp)} + \Delta LW^{(WV)}$$
$$+ \Delta LW^{(CLD)} + \Delta LW^{(BC)} + \Delta LW^{(OC)} \tag{5}$$
$$+ \Delta LW^{(SULF)} + \Delta LW^{(SS)} + \Delta LW^{(DUST)} + \Delta res_{LW}$$

In the Eqs. (4) and (5), superscripts SR, O₃, Temp, AL, WV, CLD, BC, OC, SULF, SS, and DUST stand for solar irradiance, ozone, temperature, surface albedo, water vapor, cloud, black carbon, organic carbon, sulfate, sea salt, and dust, respectively. Δres_{SW} and Δres_{LW} are the budget residuals, which are obtained by subtracting all right-hand-side terms from the left-hand-side term in Eqs. (4) and (5). The residual terms inevitably include errors associated with the offline radiative transfer calculation, linearization, and forcings not explicitly considered (e.g., CO_2, CH_4, and N_2O). The sum of ΔSW and ΔLW represents the net radiative flux. The sum of energy perturbations associated with black carbon, organic carbon, sulfate, sea salt, and dust represent the aerosol effect. The vertical profile of the differences in net shortwave and longwave radiative fluxes at a given location between two states can be decomposed into the vertical profile of partial radiative flux differences due to the changes in individual radiative processes listed above. Note that the partial radiative flux changes associated with aerosols are results from the direct radiative effects, while the indirect effects of aerosols are included in the radiative flux changes associated with clouds. All the terms in the Eqs. (2–5) have units of watts per meter square (W m^{-2}).

Following Zhang et al. [37], the Rapid Radiative Transfer Method for general circulation model version 5[69] and the Monte Carlo integration of the Independent Column Approximation[70] method with maximum-random overlap cloud generator are employed to obtain the individual shortwave and longwave radiative energy perturbations in the Eqs. (4) and (5) by conducting offline radiative transfer calculations separately for state "A" and state "B" associated with different radiative processes (details referred to Chen et al. [35]). The aerosol optical properties of five types of aerosols (e.g., asymmetry parameter, single-scatter albedo, absorption, and extinction) are adopted from the four-mode version of the Modal Aerosol Model[71].

The input variables required by the PREAF calculation include surface/air temperature, zonal, meridional, and vertical velocities, specific humidity, geopotential height, solar irradiance at the top of the atmosphere, surface net downward shortwave/longwave radiative flux, surface albedo, surface latent/sensible heat flux, ozone mixing ratio, cloud amount, cloud liquid/ice water content, black carbon/organic carbon/sulfate/sea salt/dust mixing ratio, and surface pressure. State "B" refers to the daily mean from 24 July 2022 to 12 September 2022 in the analysis using the MERRA-2 and from 27 July 2022 to 6 September 2022 in the analysis using the CFSv2. The corresponding state "A" refers to the daily climatology defined in the "Climatology" section. The 3-hourly variables from the MERRA-2 and the 6-hourly variables from the CFSv2 are served as the inputs to solve Eqs. (2) and (3). Due to the low temporal resolution of the input variables, the estimation of horizontal advection inevitably includes large errors. Therefore, it is calculated as the residual of all other budget terms in Eq. (2). The change in total energy tendency of land surface in the left-hand side of Eq. (3) is calculated as the sum of right-hand-side budget terms. The daily mean variables serve as the input for the offline radiative transfer calculations to obtain the energy perturbations associated with individual radiative

processes in Eqs. (4) and (5). Note that an aerosol module is missing in the CFSv2 model, and thus the radiative effect of aerosols is not calculated for the CFSv2 prediction. The use of time-mean cloud properties in radiative transfer calculations leads to large biases in estimating cloud radiative effects[72,73]. To minimize the offline errors, $\Delta SW^{(CLD)}$ and $\Delta LW^{(CLD)}$ are estimated as the changes in differences between surface net downward shortwave/longwave radiative flux under all sky and clear sky[74], which are the direct outputs from the MERRA-2 and the CFSv2. Δres_{SW} and Δres_{LW} at the land surface are calculated by subtracting all terms on the right-hand side of Eqs. (4) and (5) derived from offline radiative calculations, from the directly estimated changes in surface net downward shortwave and longwave radiative fluxes from the MERRA-2 and the CFSv2. Δres_{SW} and Δres_{LW} are included in the atmospheric horizontal advection term estimated as a residual in the Eq. (2) for the atmospheric layers. The surface friction is negligible in this study.

DATA AVAILABILITY

The CPC temperature and precipitation are publicly available at https://psl.noaa.gov/data/gridded/data.cpc.globaltemp.html and https://psl.noaa.gov/data/gridded/data.cpc.globalprecip.html, respectively. The GLEAM and the MERRA-2 are publicly available at https://www.gleam.eu and https://disc.gsfc.nasa.gov/datasets?page=1&project=MERRA-2, respectively. The MODIS products from Aqua (MYD08_L3) and Terra (MOD08_L3) are publicly available at https://ladsweb.modaps.eosdis.nasa.gov/missions-and-measurements/products/MYD08_D3 and https://ladsweb.modaps.eosdis.nasa.gov/missions-and-measurements/products/MOD08_D3. The NCEP CFSv2 forecast is publicly available at https://www.ncei.noaa.gov/products/weather-climate-models/climate-forecast-system.

CODE AVAILABILITY

The Rapid Radiative Transfer Method for general circulation model version 5 can be obtained from the Atmospheric and Environmental Research (https://github.com/AER-RC). All figures in this paper are produced by the NCAR Command Language (NCL) version 6.6.2, and the source codes can be obtained upon request to the corresponding author.

REFERENCES

1. Robine, J.-M. et al. Death toll exceeded 70,000 in Europe during the summer of 2003. C. R. Biol. **331**, 171–178 (2008).
2. Brown, A. Heatwave mortality. Nat. Clim. Change **6**, 821–821 (2016).
3. Baldwin, J. W., Dessy, J. B., Vecchi, G. A. & Oppenheimer, M. Temporally Compound heat wave events and global warming: an emerging hazard. Earth's Future **7**, 411–427 (2019).
4. Wang, J. et al. Anthropogenic emissions and urbanization increase risk of compound hot extremes in cities. Nat. Clim. Change **11**, 1084–1089 (2021).
5. Mukherjee, S., Mishra, A. K., Zscheischler, J. & Entekhabi, D. Interaction between dry and hot extremes at a global scale using a cascade modeling framework. Nat. Commun. **14**, 277 (2023).
6. Zhang, T. et al. Influences of the boreal winter Arctic Oscillation on the peak-summer compound heat waves over the Yangtze–Huaihe River basin: the North Atlantic capacitor effect. Clim. Dyn. **59**, 2331–2343 (2022).
7. Yang, X., Chen, F., Zhu, W. & Teng, W. Urbanization effects on observed changes in summer extreme heat events over Zhejiang province, East China. J. Trop. Meteorol. **21**, 295–302 (2015).
8. Wang, X., Sun, X., Tang, J. & Yang, X. Urbanization-induced regional warming in Yangtze River Delta: potential role of anthropogenic heat release. Int. J. Climatol. **35**, 4417–4430 (2015).
9. Lu, R. et al. Heat waves in summer 2022 and increasing concern regarding heat waves in general. Atmos. Ocean. Sci. Lett. **16**, 100290 (2023).
10. Mallapaty, S. China's extreme weather challenges scientists trying to study it. Nature **609**, 888 (2022).
11. Wang, Y. et al. Tens of thousands additional deaths annually in cities of China between 1.5 °C and 2.0 °C warming. Nat. Commun. **10**, 3376 (2019).
12. Perkins-Kirkpatrick, S. E. & Lewis, S. C. Increasing trends in regional heatwaves. Nat. Commun. **11**, 3357 (2020).
13. Chen, H. et al. Projections of heatwave-attributable mortality under climate change and future population scenarios in China. Lancet Reg. Health West Pac. **28**, 100582 (2022).
14. Yin, J. et al. Future socio-ecosystem productivity threatened by compound drought–heatwave events. Nat. Sustain. **6**, 259–272 (2023).
15. Wang, Z., Luo, H. & Yang, S. Different mechanisms for the extremely hot central-eastern China in July-August 2022 from a Eurasian large-scale circulation perspective. Environ. Res. Lett. **18**, 024023 (2023).
16. He, C., Zhou, T., Zhang, L., Chen, X. & Zhang, W. Extremely hot East Asia and flooding western South Asia in the summer of 2022 tied to reversed flow over Tibetan Plateau. Clim. Dyn. **61**, 2103–2119 (2023).
17. Jiang, J., Liu, Y., Mao, J. & Wu, G. Extreme heatwave over eastern China in summer 2022: the role of three oceans and local soil moisture feedback. Environ. Res. Lett. **18**, 044025 (2023).
18. Zhang, D., Chen, L., Yuan, Y., Zuo, J. & Ke, Z. Why was the heat wave in the Yangtze River valley abnormally intensified in late summer 2022? Environ. Res. Lett. **18**, 034014 (2023).
19. Tang, S. et al. Linkages of unprecedented 2022 Yangtze River Valley heatwaves to Pakistan flood and triple-dip La Niña. npj Clim. Atmos. Sci. **6**, 44 (2023).
20. Liu, B., Zhu, C., Ma, S., Yan, Y. Jiang, N. Subseasonal processes of triple extreme heatwaves over the Yangtze River Valley in 2022. Weather Clim. Extrem. **40**, 100572 (2023).
21. Miralles, D. G., Teuling, A. J., van Heerwaarden, C. C. & Vilà-Guerau de Arellano, J. Mega-heatwave temperatures due to combined soil desiccation and atmospheric heat accumulation. Nat. Geosci. **7**, 345–349 (2014).
22. Luo, M. & Lau, N.-C. Heat Waves in Southern China: Synoptic behavior, long-term change, and urbanization effects. J. Clim. **30**, 703–720 (2017).
23. Zscheischler, J. et al. A typology of compound weather and climate events. Nat. Rev. Earth Environ. **1**, 333–347 (2020).
24. Ha, K.-J. et al. Dynamics and characteristics of dry and moist heatwaves over East Asia. npj Clim. Atmos. Sci. **5**, 1–11 (2022).
25. Seo, Y.-W., Ha, K.-J. & Park, T.-W. Feedback attribution to dry heatwaves over East Asia. Environ. Res. Lett. **16**, 064003 (2021).
26. Yu, B., Lin, H., Mo, R. & Li, G. A physical analysis of summertime North American heatwaves. Clim. Dyn. **61**, 1551–1565 (2023).
27. Fischer, E. M., Seneviratne, S. I., Vidale, P. L., Lüthi, D. & Schär, C. Soil moisture–atmosphere interactions during the 2003 European summer heat wave. J. Clim. **20**, 5081–5099 (2007).
28. Péré, J. C., Mallet, M., Pont, V. & Bessagnet, B. Impact of aerosol direct radiative forcing on the radiative budget, surface heat fluxes, and atmospheric dynamics during the heat wave of summer 2003 over western Europe: A modeling study. J. Geophys. Res. Atmos. **116**, D23119 (2011).
29. Zhai, P., Zhou, B. & Chen, Y. A review of climate change attribution studies. J. Meteorol. Res. **32**, 671–692 (2018).
30. Wetherald, R. T. & Manabe, S. Cloud feedback processes in a General Circulation Model. J. Atmos. Sci. **45**, 1397–1416 (1988).
31. Cai, M. & Lu, J. A new framework for isolating individual feedback processes in coupled general circulation climate models. Part II: Method demonstrations and comparisons. Clim. Dyn. **32**, 887–900 (2008).
32. Lu, J. & Cai, M. A new framework for isolating individual feedback processes in coupled general circulation climate models. Part I: Formul. Clim. Dyn. **32**, 873–885 (2009).
33. Taylor, K. E. et al. Estimating Shortwave radiative forcing and response in climate models. J. Clim. **20**, 2530–2543 (2007).
34. Colman, R. A. Climate radiative feedbacks and adjustments at the Earth's surface. J. Geophys. Res. Atmos. **120**, 3173–3182 (2015).
35. Chen, J., Deng, Y., Lin, W. & Yang, S. A process-based assessment of decadal-scale surface temperature evolutions in the NCAR CCSM4's 25-year hindcast experiments. J. Clim. **30**, 6723–6736 (2017).
36. Chen, J., Deng, Y., Lin, W. & Yang, S. A process-based decomposition of decadal-scale surface temperature evolutions over East Asia. Clim. Dyn. **51**, 4371–4383 (2018).
37. Zhang, T., Deng, Y., Chen, J., Gao, P. & Zhang, H. Disentangling physical and dynamical drivers of the 2016/17 record-breaking warm winter in China. Environ. Res. Lett. **17**, 074024 (2022).
38. Neelin, J. D. & Held, I. M. Modeling tropical convergence based on the moist static energy budget. Mon. Wea. Rev. **115**, 3–12 (1987).
39. Maloney, E. D. The moist static energy budget of a composite tropical intraseasonal oscillation in a climate model. J. Clim. **22**, 711–729 (2009).
40. Maloney, E. D., Sobel, A. H. & Hannah, W. M. Intraseasonal variability in an aquaplanet General Circulation Model. J. Adv. Model. Earth Syst. **2**, 5 (2010).
41. Wang, S. & Sobel, A. H. A unified moisture mode theory for the Madden–Julian Oscillation and the Boreal Summer Intraseasonal Oscillation. J. Clim. **35**, 1267–1291 (2022).

42. Sun, D.-Z. & Trenberth, K. E. Coordinated heat removal from the equatorial Pacific during the 1986-87 El Niño. *Geophy. Res. Lett.* **25**, 2659–2662 (1998).

43. Soden, B. J. & Held, I. M. An assessment of climate feedbacks in coupled ocean–atmosphere models. *J. Clim.* **19**, 3354–3360 (2006).

44. Soden, B. J. et al. Quantifying climate feedbacks using radiative kernels. *J. Clim.* **21**, 3504–3520 (2008).

45. Hu, X., Cai, M., Yang, S. & Wu, Z. Delineation of thermodynamic and dynamic responses to sea surface temperature forcing associated with El Niño. *Clim. Dyn.* **51**, 4329–4344 (2017).

46. Hu, X. et al. Decadal evolution of the surface energy budget during the fast warming and global warming hiatus periods in the ERA-interim. *Clim. Dyn.* **52**, 2005–2016 (2018).

47. Hu, X., Sejas, S., Cai, M., Li, Z. & Yang, S. Atmospheric dynamics footprint on the January 2016 ice sheet melting in West Antarctica. *Geophy. Res. Lett.* **46**, 2829–2835 (2019).

48. Jenkins, M. & Dai, A. The impact of sea-ice loss on Arctic climate feedbacks and their role for Arctic amplification. *Geophy. Res. Lett.* **48**, e2021GL094599 (2021).

49. Terray, L. A storyline approach to the June 2021 northwestern North American heatwave. *Geophy. Res. Lett.* **50**, e2022GL101640 (2023).

50. Hsu, C. J. & Plumb, R. A. Nonaxisymmetric thermally driven circulations and upper-tropospheric monsoon dynamics. *J. Atmos. Sci.* **57**, 1255–1276 (2000).

51. Siu, L. W. & Bowman, K. P. Unsteady vortex behavior in the Asian monsoon anticyclone. *J. Atmos. Sci.* **77**, 4067–4088 (2020).

52. Wang, X., Randel, W., Pan, L., Wu, Y. & Zhang, P. Transient behavior of the Asian summer monsoon anticyclone associated with eastward eddy shedding. *J. Geophys. Res. Atmos.* **127**, e2021JD036090 (2022).

53. Hsu, P.-C., Qian, Y., Liu, Y., Murakami, H. & Gao, Y. Role of Abnormally Enhanced MJO over the Western Pacific in the Formation and Subseasonal Predictability of the Record-Breaking Northeast Asian Heatwave in the Summer of 2018. *J. Clim.* **33**, 3333–3349 (2020).

54. Meng, W. et al. Application of WRF/UCM in the simulation of a heat wave event and urban heat island around Guangzhou. *J. Trop. Meteorol.* **17**, 257–267 (2011).

55. Ford, T. W., Dirmeyer, P. A. & Benson, D. O. Evaluation of heat wave forecasts seamlessly across subseasonal timescales. *npj Clim. Atmos. Sci.* **1**, 20 (2018).

56. Sun, D.-Z. & Held, I. M. A comparison of modeled and observed relationships between interannual variations of water vapor and temperature. *J. Clim.* **9**, 665–675 (1996).

57. Chen, M. et al. Assessing objective techniques for gauge-based analyses of global daily precipitation. *J. Geophys. Res. Atmos.* **113**, D04110 (2008).

58. McKee, T. B., Doesken, N. J. & Kleist, J. The relationship of drought frequency and duration on time scales. *Eighth Conference on Applied Climatology, Anaheim, California, Jan 17–23,* 179–186 (American Meteorological Society, 1993).

59. McKee, T. B., Doesken, N. J. & Kleist, J. Drought monitoring with multiple time scales. *Ninth Conference on Applied Climatology, Dallas, Texas, Jan 15–20,* 233–236 (American Meteorological Society, 1995).

60. Miralles, D. G. et al. Global land-surface evaporation estimated from satellite-based observations. *Hydrol. Earth Syst. Sci.* **15**, 453–469 (2011).

61. Martens, B. et al. GLEAM v3: satellite-based land evaporation and root-zone soil moisture. *Geosci. Model Dev.* **10**, 1903–1925 (2017).

62. Platnick, S. et al. MODIS Atmosphere L3 Daily Product. NASA MODIS Adaptive Processing System, Goddard Space Flight Center, USA: https://doi.org/10.5067/MODIS/MYD08_D3.061 (2014).

63. Gelaro, R. et al. The Modern-Era Retrospective Analysis for Research and Applications, Version 2 (MERRA-2). *J. Clim.* **30**, 5419–5454 (2017).

64. Draper, C. S., Reichle, R. H. & Koster, R. D. Assessment of MERRA-2 land Surface energy flux estimates. *J. Clim.* **31**, 671–691 (2018).

65. Zhang, T., Zang, L., Mao, F., Wan, Y. & Zhu, Y. Evaluation of Himawari-8/AHI, MERRA-2, and CAMS Aerosol Products over China. *Remote Sensing.* **12**, 1684 (2020).

66. Du, J., Wang, K., Wang, J., Jiang, S. & Zhou, C. Diurnal cycle of surface air temperature within China in current reanalyses: Evaluation and diagnostics. *J. Clim.* **31**, 4585–4603 (2018).

67. Reichle, R. H. et al. Land surface precipitation in MERRA-2. *J. Clim.* **30**, 1643–1664 (2017).

68. Saha, S. et al. The NCEP Climate Forecast System Version 2. *J. Clim.* **27**, 2185–2208 (2014).

69. Iacono, M. J. et al. Radiative forcing by long-lived greenhouse gases: Calculations with the AER radiative transfer models. *J. Geophys. Res. Atmos.* **113**, D13103 (2008).

70. Pincus, R., Barker, H. W. & Morcrette, J.-J. A fast, flexible, approximate technique for computing radiative transfer in inhomogeneous cloud fields. *J. Geophys. Res. Atmos.* **108**, 4376 (2003).

71. Liu, X. et al. Description and evaluation of a new four-mode version of the Modal Aerosol Module (MAM4) within version 5.3 of the Community Atmosphere Model. *Geosci. Model Dev.* **9**, 505–522 (2016).

72. Sejas, S. A. et al. Individual feedback contributions to the seasonality of surface warming. *J. Clim.* **27**, 5653–5669 (2014).

73. Song, X., Zhang, G. J. & Cai, M. Characterizing the climate feedback pattern in the NCAR CCSM3-SOM using hourly data. *J. Clim.* **27**, 2912–2930 (2014).

74. Chen, T., Rossow, W. B. & Zhang, Y. Radiative effects of cloud-type variations. *J. Clim.* **13**, 264–286 (2000).

AUTHOR CONTRIBUTIONS

J.C. conceived the idea for the study, and T.Z. drafted the paper. J.C. and T.Z. downloaded the data and performed the calculations. All authors discussed the results throughout the whole process. Y.D. and S.Y. contributed to the revision.

COMPETING INTERESTS

The authors declare no competing interests.

ADDITIONAL INFORMATION

Supplementary information The online version contains supplementary material available at https://doi.org/10.1038/s41612-023-00490-4.

Correspondence and requests for materials should be addressed to Junwen Chen.

Reprints and permission information is available at http://www.nature.com/reprints

Publisher's note Springer Nature remains neutral with regard to jurisdictional claims in published maps and institutional affiliations.